AIAA JOURNAL
Vol. 46, No. 8, August 2008

Discontinuous Galerkin Multimodel Methods for Optimal Control of Aeroacoustics

Guoquan Chen*
Rice University, Houston, Texas 77005-1892
and
S. Scott Collis†
Sandia National Laboratories, Albuquerque, New Mexico 87185-1320

DOI: 10.2514/1.23798

A new multimodel computational framework for optimal control of aeroacoustic noise is presented using a near-field compressible Navier–Stokes solver coupled with a far-field linearized Euler solver, both based on a discontinuous Galerkin formulation. In this approach, the coupling of near- and far-field domains is achieved by weakly enforcing continuity of normal fluxes across a coupling surface that encloses all nonlinearities and noise sources. For optimal control, gradient information is obtained by the solution of an appropriate adjoint problem that involves the propagation of adjoint information from the far field to the near field. This computational framework is applied to study optimal boundary control of blade–vortex interaction, which is a significant noise source for helicopters on approach to landing. In the prototype problem presented here, the noise propagated toward the ground is reduced by 12 dB, demonstrating the potential of an optimization-based approach to blade–vortex-interaction noise control.

Nomenclature

$\mathbf{F}$	=	inviscid flux vector
$\mathbf{F}^v$	=	viscous flux vector
g	=	control defined on the rotor blade
J	=	objective functional
M_∞	=	freestream Mach number
p'	=	pressure fluctuations in the observation region
$\boldsymbol{Q}$	=	auxiliary variables in the far-field domain
$\mathbf{U}$	=	conservative flow variables in the near-field domain
$\mathbf{Y}$	=	primitive flow variables in the near-field domain
$\bar{\mathbf{Y}}$	=	mean-flow primitive variables
$\mathbf{y}$	=	fluctuations in the primitive variables in the far-field domain
Γ_c	=	coupling boundary between two subdomains
Γ_g	=	control region
$\boldsymbol{\lambda}$	=	adjoint variables in the near-field domain
$\boldsymbol{\xi}$	=	adjoint variables in the far-field domain
Ω_{far}	=	far-field domain
Ω_{near}	=	near-field domain
Ω_{obs}	=	observation region

Introduction

THE coupling of accurate computational fluid dynamics analysis with optimal control theory has the potential to advance active flow control for complex flows, including flows involving aeroacoustic noise generation. In this paper, we report on progress in extending our previous work [1,2] on aeroacoustic control by using a multimodel approach for optimal control of aeroacoustics. Our goal is to develop effective numerical methods to investigate the feasibility of using wall-normal actuation for controlling blade–vortex interaction (BVI). Rotorcraft blade–vortex interaction typically occurs at low-speed descending flight conditions (such as on approach to landing) and produces high-amplitude impulsive noise that often dominates other noise sources [3–16]. Reduction of BVI noise may alleviate restrictions on civil rotorcraft use near city centers and thereby enhance community acceptance.

We have developed an optimal control framework for aeroacoustic applications that can help to identify novel strategies for controlling BVI noise in a systematic manner. The main purpose of aeroacoustic computations is to determine the sound intensity and directivity far away from the noise source. However, the computational cost of using a high-fidelity flow-physics model across such a large domain is usually prohibitive and most researchers have resorted to some form of multiphysics domain-decomposition method [17]. For example, in Fig. 1 the near field is obtained by numerical solution of the Navier–Stokes equations, whereas far away from the noise source, where the effects of nonlinearities are negligible, the linearized Euler equations or isentropic wave equations can be used to model the propagating acoustic waves. The interface between the near-field and far-field regions can be accomplished by using a Kirchhoff-type method [18,19], Lighthill theory and its derivatives [20,21], or by a direct solution of the linearized Euler equations [22–25]. In this paper, our focus is on the formulation and implementation of multimodel/multidomain methods for adjoint-based optimal control of aeroacoustics with specific application to BVI noise control.

Problem Formulation

Our previous research has included adjoint-based optimal control of the unsteady compressible Navier–Stokes and Euler equations [1,26–29], as well as optimal control of unsteady flows discretized using the discontinuous Galerkin (DG) method [2]. Here, we present a multidomain/multimodel formulation based on DG discretizations for both the state and adjoint, for use in optimal control. In this approach, the coupling of multidomains (near field and far field) and multimodels is achieved by weakly enforcing continuity of normal fluxes across a coupling surface using a discontinuous Galerkin approach. The goal of multidomain/multimodel simulation is to

Presented as Paper 0410 at the 43rd AIAA Aerospace Sciences Meeting, Reno, NV, 10 January 2005–13 January 2006; received 11 March 2006; revision received 7 March 2008; accepted for publication 8 April 2008.

*Department of Mechanical Engineering and Materials Science; currently Ion Geophysical, Houston, TX 77042; guoquan.chen@iongeo.com. Member AIAA.

†Manager, Scalable Algorithms; sscoll@sandia.gov. Senior Member AIAA.

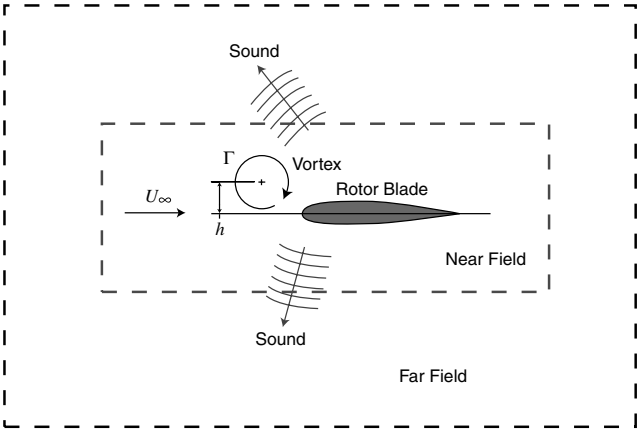

Fig. 1 Blade–vortex interaction.

reduce the overall computational cost of flow simulation by using locally less expensive and more computationally efficient physical models without sacrificing the global fidelity of the simulation. Our objective is to develop multimodel simulations using a discontinuous Galerkin spatial discretization for the state and adjoint equations and to use this method within gradient-based optimization algorithms to obtain optimal temporal and spatial distributions of boundary actuation so as to minimize far-field sound.

The control objective for the problems presented here targets acoustic waves that are typically several orders of magnitude smaller than the mean flow. This makes linearized methods, such as the linearized Euler equations or the wave equation, appropriate methods for acoustic propagation in the far field. Because we specifically focus on blowing and suction on the surface of the rotor blade, which may introduce vorticity at the blade surface, we use the Navier–Stokes equations in the near field to capture this potentially viscous phenomenon.[‡] However, the use of Navier–Stokes in the near-field limits our current computations to relatively low Reynolds numbers for idealized two-dimensional BVI model problems; our future work will focus on extending these methods toward more realistic BVI scenarios.

We begin in the following subsection by discussing details of the state and adjoint coupling for this multidomain/multimodel system, and the remainder of the current section focuses on the formulation for the state, optimal control problem, and resulting adjoint equations. To simplify the presentation, the discussion is limited to a system that has only two subdomains (i.e., near field and far field), where the Navier–Stokes equations are solved in the near field and the linearized Euler equations are solved in the far field. However, both our formulation and implementation allow for an arbitrary number of subdomains with a variety of physical models, including Navier–Stokes, Euler, linearized Navier–Stokes, linearized Euler, and wave equations, and the interested reader should consult [30].

State Equations

The computational domain Ω is divided into two subdomains: Ω_{near} in the near field and Ω_{far} in the far field. The coupling boundary between these two subdomains is referred to as Γ_c. In the near field, the flow is modeled using the compressible Navier–Stokes equations in conservative form, which are given by

$$\mathbf{U}_{,t}(\mathbf{Y}) + \mathbf{F}_{i,i}(\mathbf{Y}) - \mathbf{F}^v_{i,i}(\mathbf{Y}, \nabla\mathbf{Y}) = \mathbf{0} \tag{1a}$$

in $(t_0, t_f) \times \Omega_{\text{near}}$ with boundary conditions

$$\mathbf{B}_{\text{near}}(\mathbf{Y}, g) = \mathbf{0} \quad \text{on } (t_0, t_f) \times \partial\Omega_{\text{near}} \tag{1b}$$

where $\mathbf{B}_{\text{near}}$ includes the coupling between near- and far-field subdomains, as well as the transpiration boundary condition on the rotor blade, and g is the control variable that is selected here to be the wall-normal velocity on the rotor blade. The initial conditions in the near field are

$$\mathbf{Y}(t_0, \mathbf{x}) = \mathbf{Y}_0(\mathbf{x}) \quad \text{in } \Omega_{\text{near}} \tag{1c}$$

where $\mathbf{Y}_0$ is typically a steady-state solution of the Navier–Stokes equations over the rotor blade, with a superimposed vortex upstream of the blade, as shown schematically in Fig. 1. In Eq. (1), $\mathbf{Y} = (\rho, u_1, u_2, T)^{\mathcal{T}}$ is the vector of primitive flow variables, and the conservative variables, expressed as functions of the primitive variables, are given by $\mathbf{U}(\mathbf{Y}) = (\rho, \rho u_1, \rho u_2, \rho E)^{\mathcal{T}}$.

The far-field flow in Ω_{far} is modeled using the linearized Euler equations. We assume that $\mathbf{Y} = \bar{\mathbf{Y}} + \mathbf{y}$, where $\bar{\mathbf{Y}}$ are mean-flow primitive variables and $\mathbf{y}$ are fluctuations in the primitive variables. With this notation, the linearized Euler equations are

$$\bar{\mathbf{M}}\mathbf{y}_{,t} + (\bar{\mathbf{A}}_i\bar{\mathbf{M}}\mathbf{y})_{,i} = \mathbf{0} \quad \text{in } (t_0, t_f) \times \Omega_{\text{far}} \tag{2}$$

where

$$\bar{\mathbf{M}}(\bar{\mathbf{Y}}) = \left.\frac{\partial \mathbf{U}}{\partial \mathbf{Y}}\right|_{\bar{\mathbf{Y}}}, \qquad \bar{\mathbf{A}}_i(\bar{\mathbf{Y}}) = \left.\frac{\partial \mathbf{F}_i}{\partial \mathbf{U}}\right|_{\mathbf{U}(\bar{\mathbf{Y}})}$$

to discretize this equation using the discontinuous Galerkin method, we introduce the variables $\boldsymbol{Q}(\mathbf{y}; \bar{\mathbf{Y}}) = \bar{\mathbf{M}}(\bar{\mathbf{Y}})\mathbf{y}$ and recast the linearized Euler equations in the form

$$\boldsymbol{Q}_{,t}(\mathbf{y}) + \mathbf{F}'_{i,i}(\mathbf{y}) = \mathbf{0} \quad \text{in } (t_0, t_f) \times \Omega_{\text{far}} \tag{3a}$$

where the flux is given by $\mathbf{F}'_i(\mathbf{y}) = \bar{\mathbf{A}}_i\boldsymbol{Q}(\mathbf{y})$. Equation (3a) is solved subject to boundary conditions of the form

$$\mathbf{B}_{\text{far}}(\mathbf{y}) = \mathbf{0} \quad \text{on } (t_0, t_f) \times \partial\Omega_{\text{far}} \tag{3b}$$

For the problems presented here, the far-field equations are not explicitly dependent on the control variable g, which lives on the rotor blade surface. However, $\mathbf{B}_{\text{far}}$ does represent the coupling between the near- and far-field subdomains, as well as nonreflecting boundary conditions on the outer, far-field, boundary. Initial conditions for the far-field problem are of the form

$$\mathbf{y}(t_0, \mathbf{x}) = \mathbf{y}_0(\mathbf{x}) \quad \text{in } \Omega_{\text{far}} \tag{3c}$$

where $\mathbf{y}_0$ is typically zero and $\bar{\mathbf{Y}}$ is the steady-state solution of the Navier–Stokes equations over the rotor blade. In the following, we suppress the explicit dependence of far-field quantities on $\bar{\mathbf{Y}}$, unless necessary for clarity.

Given the similarity of Eqs. (1) and (3), we are able to solve these equations in a unified discontinuous Galerkin framework that is particularly convenient for multimodel simulation and optimization.

Optimal Control Problem

In our optimal control formulation, we seek to minimize the following objective function:

$$J(\mathbf{y}, g) = \frac{\alpha}{2}\int_{t_0}^{t_f}\int_{\Omega_{\text{obs}}} (p')^2 \,\mathrm{d}\mathbf{x}\,\mathrm{d}t + \frac{1}{2}\int_{t_0}^{t_f}\int_{\Gamma_g} g^2 \,\mathrm{d}\Gamma\,\mathrm{d}t \tag{4}$$

where $p'(\mathbf{x})$ are pressure fluctuations in the observation region and the penalty factor $\alpha = 10^3$ for the problems considered here.[§] The objective is to minimize the acoustic pressure intensity in $\Omega_{\text{obs}} \subset \Omega_{\text{far}}$ within the time horizons t_0 and t_f. Recall that the control g is chosen to be the time- and position-dependent wall-normal velocity on the surface of the rotor blade Γ_g.

[‡]Once the control is computed, we evaluate whether the control is primarily inviscid or viscous in nature. However, for this initial study, we do not want to a priori constrain the control to be inviscid.

[§]In practice, the selection of α is based on engineering judgment concerning the relative cost of the control, and in our model problems, this parameter was set based on numerical experimentation to obtain sufficient control authority with modest control power input.

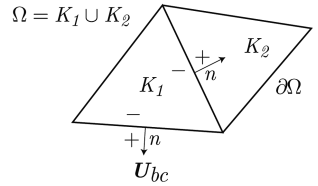

Fig. 2 Schematic of DG discretization, the solution and weighting functions are discontinuous across element interfaces.

Adjoint Equations

We use a gradient-based optimization procedure to solve the optimal control problem represented by minimizing Eq. (4) subject to state equation (1) in the near field and state equation (3) in the far field. The gradient is computed using a continuous adjoint method (i.e., the optimize-then-discretize approach), as introduced by Joslin et al. [31]. Because of space limitations, we only present a summary of the formulation here and the interested reader should consult [30] for more details.

We begin by introducing the adjoint variables $\boldsymbol{\lambda}$ for the near-field Navier–Stokes equations and $\boldsymbol{\xi}$ for the linearized Euler equations in the far field. We then define an augmented Lagrangian as

$$L(\mathbf{U}(\mathbf{Y}), \boldsymbol{Q}(\mathbf{y}), g\boldsymbol{\lambda}, \boldsymbol{\xi},) = J(\mathbf{y}, g) + \int_{t_0}^{t_f} \int_{\Omega_{\text{near}}} \boldsymbol{\lambda} \cdot (\mathbf{U}_{,t} + \mathbf{F}_{i,i} - \mathbf{F}^v_{i,i})\, \mathrm{d}\mathbf{x}\, \mathrm{d}t + \int_{t_0}^{t_f} \int_{\Omega_{\text{far}}} \boldsymbol{\xi} \cdot (\boldsymbol{Q}_{,t} + \mathbf{F}^l_{i,i})\, \mathrm{d}\mathbf{x}\, \mathrm{d}t \tag{5}$$

The optimality equations are obtained by taking appropriate variations of the Lagrangian. For example, variations with respect to $\mathbf{Y}$ lead to the adjoint Navier–Stokes equation in the near field:

$$-\boldsymbol{\lambda}_{,t} - (\mathbf{A}_i^T \boldsymbol{\lambda})_{,i} + (\hat{\mathbf{D}}_i^T \boldsymbol{\lambda})_{,i} - (\hat{\mathbf{K}}_{ij}^T \boldsymbol{\lambda}_{,j})_{,i} = \mathbf{A}_{i,i}^T \boldsymbol{\lambda} + \hat{\mathbf{D}}_{,i}^T \boldsymbol{\lambda} \quad \text{in } (t_0, t_f) \times \Omega_{\text{near}} \tag{6}$$

whereas variations of Eq. (5) with $\mathbf{y}$ yield the adjoint linearized Euler equation in the far field:

$$-\boldsymbol{\xi}_{,t} - \bar{\mathbf{A}}_i^T \boldsymbol{\xi}_{,i} = \mathbf{S} \quad \text{in } (t_0, t_f) \times \Omega_{\text{far}} \tag{7}$$

where $\mathbf{S}$ depends on the variation of the objective functional with $\mathbf{y}$ and

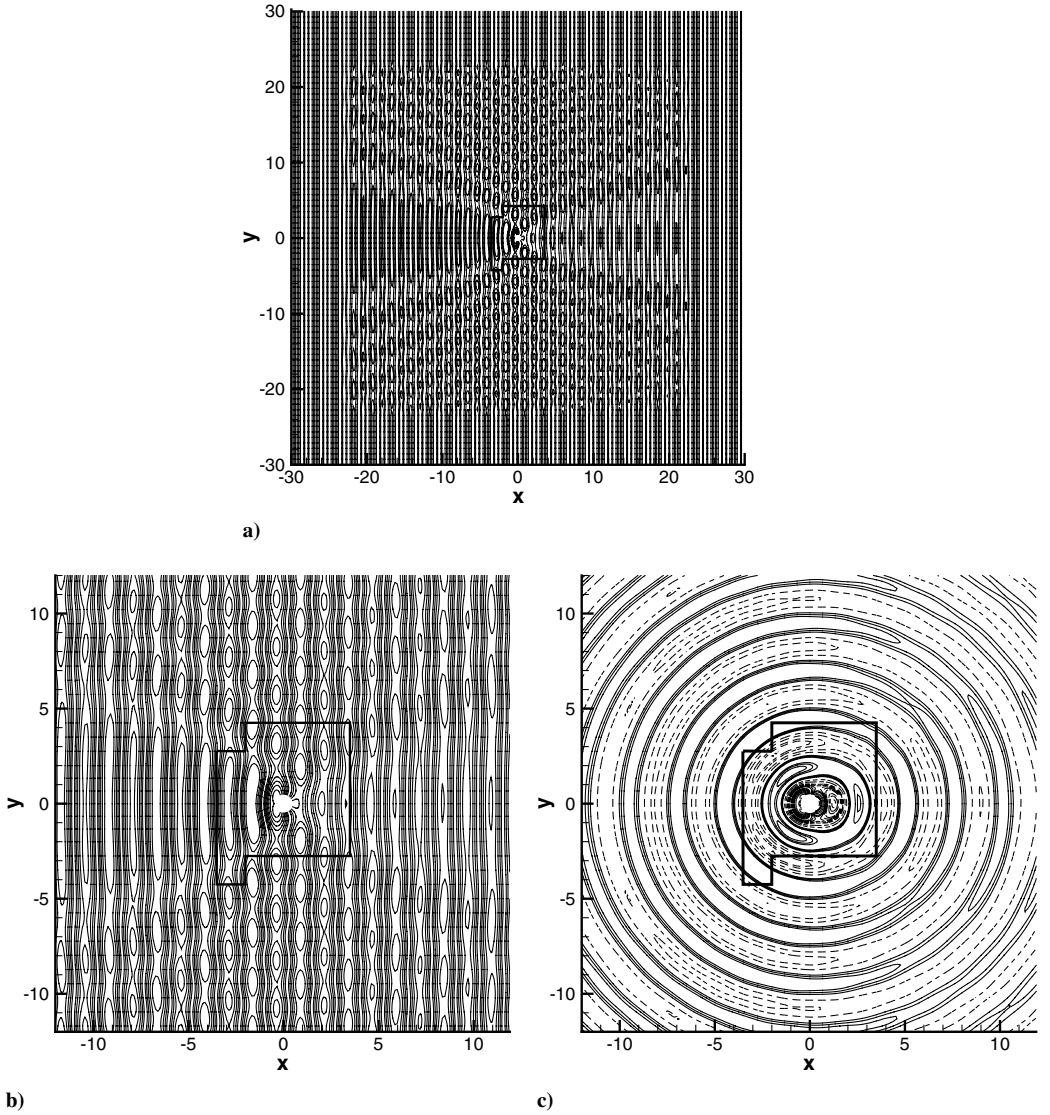

Fig. 3 Acoustic scattering from a circular cylinder: a) incident and scattered pressure on the full domain, b) incident and scattered pressure contour near the cylinder with minimum 7.9225, maximum 7.9460, and 12 contour levels, and c) scattered pressure contour near the cylinder with minimum −0.005816, maximum 0.003180, and 19 contour levels; the irregular solid line denotes the interface between the Euler region in the near field and the wave-equation region in the far field.

$$\mathbf{A}_i = \frac{\partial \mathbf{F}_i}{\partial \mathbf{U}}, \qquad \hat{\mathbf{D}}_i = \frac{\partial \mathbf{F}_i^v}{\partial \mathbf{U}}, \qquad \hat{\mathbf{K}}_j^i = \frac{\partial \mathbf{F}_i^v}{\partial \mathbf{U}_{xj}}$$

The interested reader is encouraged to refer to [30] for more details.

The adjoint equations (6) and (7) are solved subject to appropriate boundary and final-time conditions, and the reader should consult [27,28,30] for details regarding the adjoint boundary conditions on the control surface as well as the resulting gradient equations. Our focus here is primarily on the multidomain/multimodel coupling of the state and adjoint systems. In our formulation, this coupling is achieved naturally by enforcement of weak boundary conditions within a discontinuous Galerkin spatial discretization, as discussed in the next section.

Numerical Implementation

Both the state and adjoint equations are discretized in time with a fourth-order-accurate explicit Runge–Kutta method that is symmetric and therefore well suited for optimal control problems [32]. A high-order-accurate discontinuous Galerkin method is used for the spatial discretization. The discontinuous Galerkin method can be thought of as a hybrid of finite volume and finite element methods that has a number of potential advantages, including high-order accuracy on unstructured meshes, local hp refinement, weak imposition of boundary conditions, local conservation, and orthogonal hierarchical bases that support multiscale and multiphysics modeling. References [33–35] indicate that, compared with other numerical methods, the discontinuous Galerkin method offers clear advantages in terms of high accuracy and spectrally small phase and dissipation errors when applied to acoustic problems. Bismuti and Kopriva [36] also show that the discontinuous Galerkin method is efficient for aeroacoustic simulation with long-distance wave propagation. For a recent update on the status of discontinuous Galerkin, the interested reader can refer to [37]. For our current purpose, the local conservation property and weak boundary-condition enforcement capabilities of DG method are leveraged to simplify the implementation of the multimodel/multidomain approach.

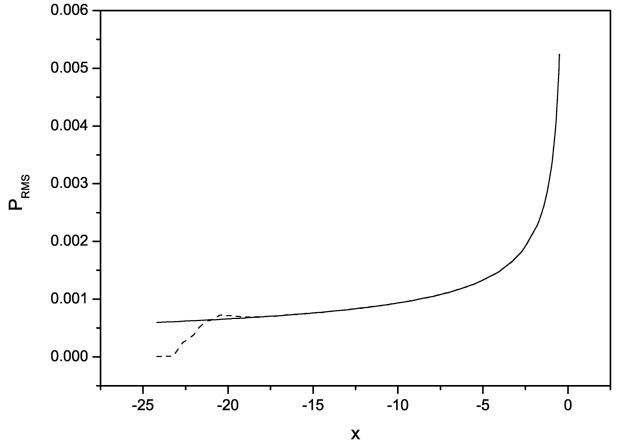

a)

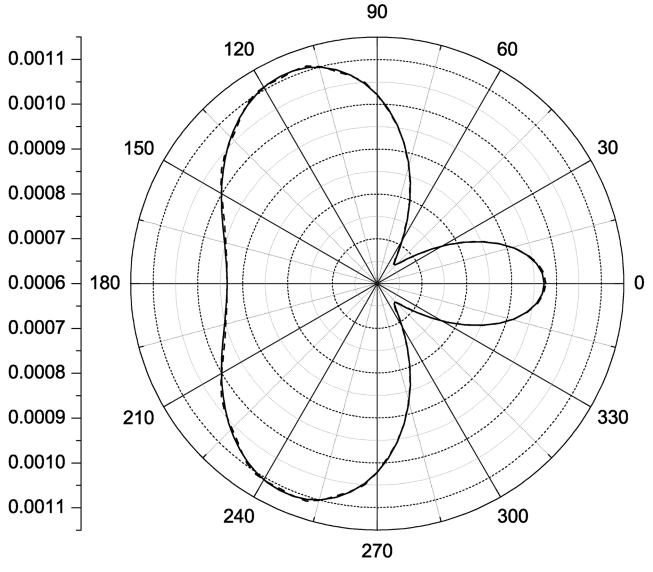

b)

Fig. 4 Acoustic scattering from a circular cylinder; comparison of rms pressure along a) ray $\theta = \pi$ and b) radius $r = 10$ (that is, outside the coupling interface); theory (solid lines) and Euler/wave (dashed lines).

Weak Formulation

The DG method for the near field is obtained by starting from the strong form of the compressible Navier–Stokes equations (1a).

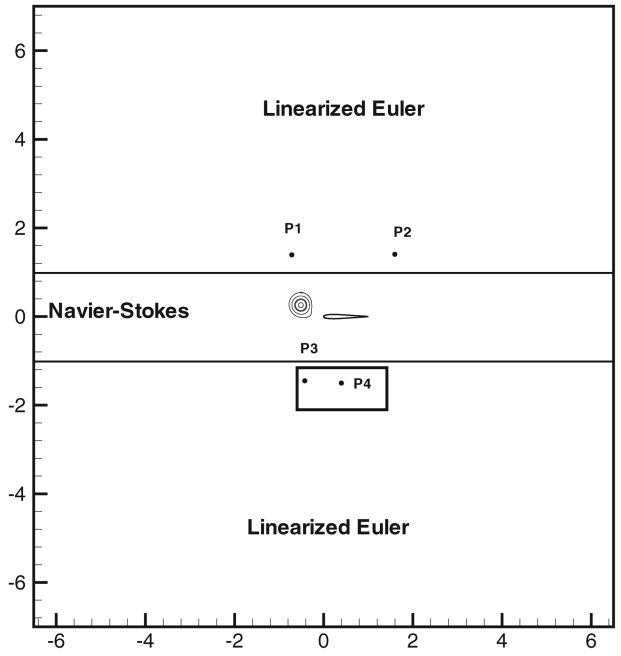

Fig. 5 Optimal control of BVI noise: problem setup.

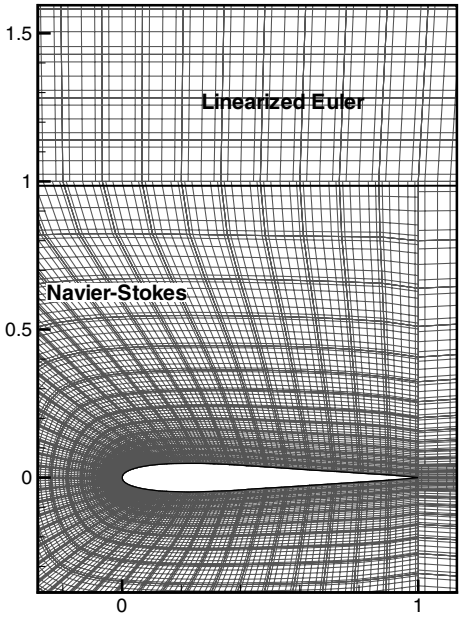

Fig. 6 Element mesh for BVI noise control.

Consider a single element K_e, multiply by a weighting function $\boldsymbol{W}$ that is continuous in K_e, integrate the flux terms by parts, replace the actual flux terms by appropriate numerical fluxes, and sum over all elements $K \in \Omega_{\text{near}}$. Doing so results in the discontinuous Galerkin weak form:

$$\sum_{e=1}^{N}\left\{\int_{K_e}(\boldsymbol{W}\cdot\mathbf{U}_{,t}+\boldsymbol{W}_{,i}\cdot(\mathbf{F}_i^v-\mathbf{F}_i))\,\mathrm{d}\mathbf{x}+\int_{\partial K_e}\boldsymbol{W}\cdot(\hat{\mathbf{F}}_n(\mathbf{U}^-,\mathbf{U}^+)-\hat{\mathbf{F}}_n^v(\mathbf{U}^-,\nabla\mathbf{U}^-,\mathbf{U}^+,\nabla\mathbf{U}^+))\,\mathrm{d}\mathbf{s}\right\}=0 \tag{8}$$

where the $\mathbf{U}^+$ and $\mathbf{U}^-$ states are defined in Fig. 2. For an element edge on the subdomain boundary $\partial\Omega_{\text{near}}$, $\mathbf{U}^+=\mathbf{U}_{\text{bc}}$ for an edge coincident with a prescribed boundary condition, or, in the case of the coupling boundary between Ω_{near} and Ω_{far}, $\mathbf{U}^+=\mathbf{U}(\bar{\mathbf{Y}}+\mathbf{y})$ on Γ_c, where $\bar{\mathbf{Y}}$ is the mean field and $\mathbf{y}$ is the far-field (perturbation) solution at that edge. Likewise, for interelement boundaries, $\mathbf{U}^+$ comes from the neighboring element. Thus, all interface and boundary conditions are set through the numerical fluxes. A Lax–Friedrichs flux is chosen for the inviscid flux $\hat{\mathbf{F}}_n$ [38] and we use the method of Bassi and Rebay [39] for the numerical viscous flux $\hat{\mathbf{F}}_n^v$.¶

The far-field linearized Euler equaitons (3a) are also discretized in space using the discontinuous Galerkin method, with the weighting function on element K_f denoted by $\boldsymbol{V}$. This leads to the DG weak form:

$$\sum_{f=1}^{M}\left\{\int_{K_f}(\boldsymbol{V}\cdot\boldsymbol{Q}_{,t}-\boldsymbol{V}_{,i}\cdot\mathbf{A}_i\boldsymbol{Q})\,\mathrm{d}\mathbf{x}+\int_{\partial\Omega_f}\boldsymbol{V}\cdot\hat{\mathbf{F}}_n'(\mathbf{y}^-,\mathbf{y}^+)\,\mathrm{d}\mathbf{s}\right\}=0 \tag{9}$$

where, again, all interface and boundary conditions are set through the numerical flux and we use a Lax–Friedrichs flux for $\hat{\mathbf{F}}_n'(\mathbf{y}^-,\mathbf{y}^+)$. For the outer far-field boundary, $\mathbf{y}^+=0$, which is a first-order nonreflecting boundary condition. On the coupling boundary Γ_c, $\mathbf{y}^+=\mathbf{Y}(\mathbf{U})-\bar{\mathbf{Y}}$, where $\mathbf{Y}(\mathbf{U})$ is the primitive solution vector corresponding to the conservative state vector $\mathbf{U}$ at the near-field edge.

Similar DG spatial discretizations are used for the adjoint equations (6) and (7), and the resulting weak forms can be found in [30]. As in the preceding state-equation coupling presented, the adjoint Navier–Stokes and adjoint linearized Euler equations are coupled through the numerical fluxes along Γ_c.

Optimization

To solve the optimization problem, the multimodel state is first solved forward in time from t_0 to t_f, and the state (both near field and far field) is stored for use in the adjoint computation. The multimodel adjoint is then solved backward in time from t_f to t_0, and the resulting adjoint solution is used to evaluate the gradient of the objective function with respect to the control. This gradient is used in a nonlinear conjugate-gradient optimization algorithm with line-search globalization. This approach is widely used in [1,27,29,40–42]. For the BVI problem presented here, we solve the optimization problem to a fairly loose tolerance (such that the change in subsequent values of J is less than about 10^{-3}). This degree of convergence is found to be sufficient for engineering purposes because the control distributions and control effectiveness do not significantly change with additional iterations.

State Validation

As validation of our multimodel state solver, we consider the classical acoustics benchmark problem of planar acoustic wave scattering from a circular cylinder. We solve this problem using our multimodel approach with the Euler equations in the near field coupled to the wave equations in the far field, and the numerical solutions are compared with the analytical result [43]. For this

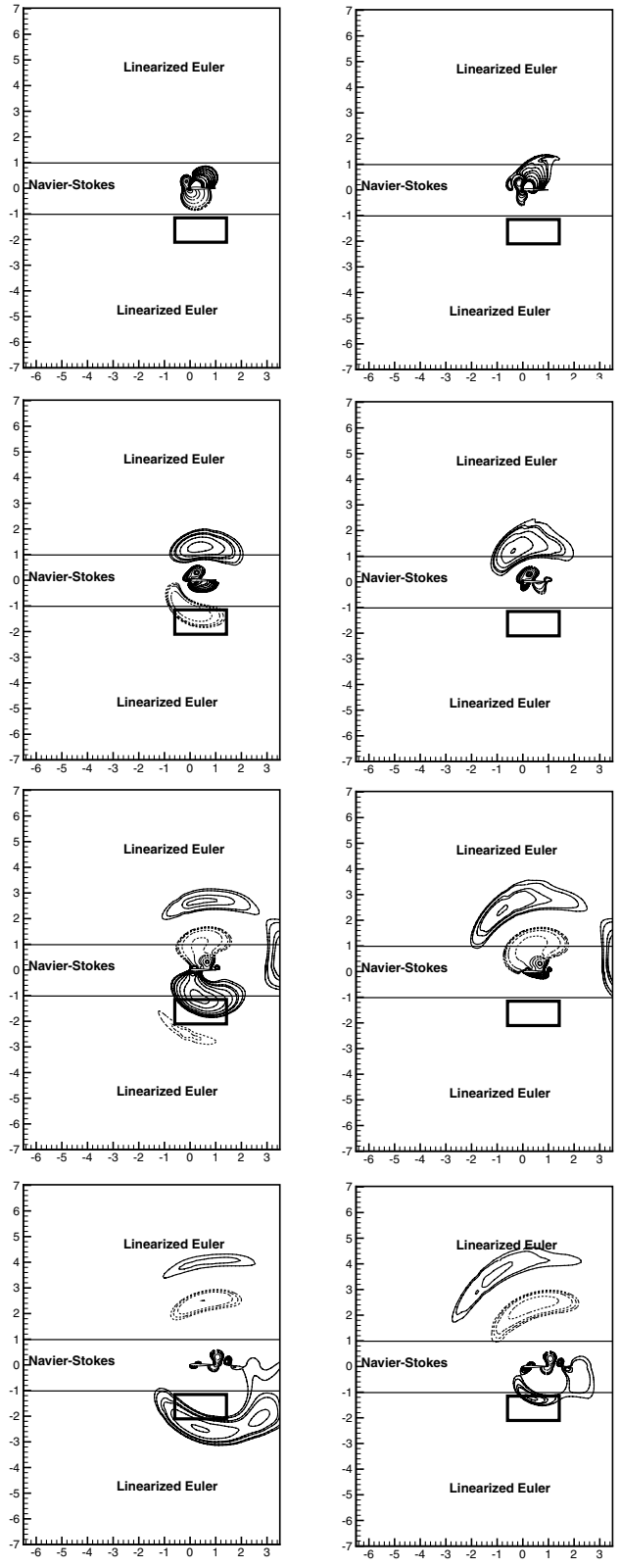

a) No control b) Optimal control

Fig. 7 Contours of scattered pressure $p-p_a$ at instants $t=5.92$, 6.32, 6.72, and 7.12 for no-control (left) and optimal control (right) with minimum −0.14906, maximum 0.03548, and 36 contour levels; positive pressure (solid lines) and negative pressure (dashed lines).

¶Although a Lax–Friedrichs flux is typically too dissipative for low-order methods, when used in DG with relatively high polynomial representations on each element $p \geq 3$, the choice of flux becomes less important and we found a simple Lax–Friedrichs to be sufficient for the high-order simulations reported here.

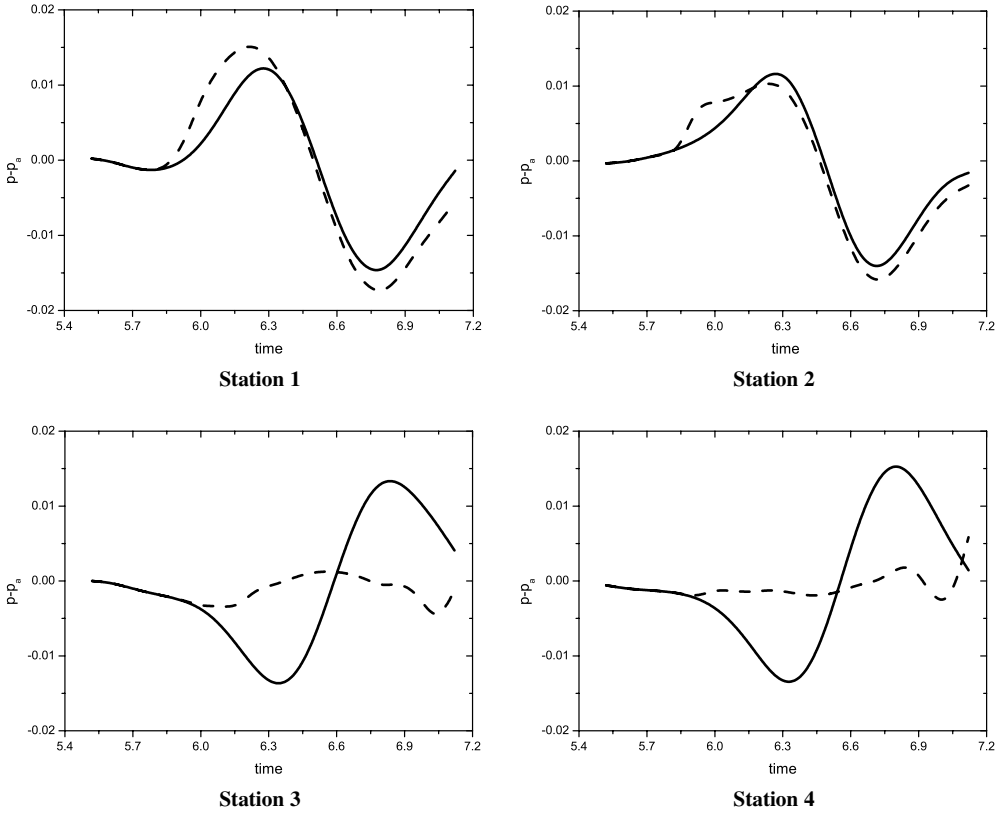

Fig. 8 Time history of pressure fluctuations at different stations; no control (solid line) and optimal control (dashed line).

calculation, the reference length is the cylinder radius, the reference velocity is the far-field sound speed, and all other reference values are based on far-field values. The incident plane wave is expressed as $p_i = P_0 \exp[ik(x - ct)]$, where the direction of propagation is along the positive x axis, and $P_0 = 0.01$ is the incident pressure amplitude. Under these conditions, the scattered pressure wave is expressed by the following Bessel function expansion [43]:

$$P_s = \sum_{m=0}^{\infty} A_m \cos(m\theta)[J_m(kr) + iN_m(kr)]e^{-i\omega t}$$

where r and θ are the usual cylindrical coordinates, $\omega = 2\pi c/\lambda$,

$$A_m = -\varepsilon_m P_0 i^{m+1} e^{-i\gamma_m} \sin(\gamma_m)$$

and $\tan(\gamma_0) = -J_1(k)/N_1(k)$.

The simulation is conducted for an incident acoustic wave with spatial wave number $k = 2.5$. The domain Ω is large $[-30, 30] \times [-30, 30]$, with a sponge layer enforced around the perimeter of the domain to approximate a nonreflecting boundary [44]. As for the mesh resolution, a block structured mesh using 6832 quadrilaterals was generated using a special-purpose grid generator [45], and each quadrilateral had polynomial order $p = 7$. From Fig. 3, it can be seen that an arbitrary interface (coincident with interelement boundaries) is selected that separates the Euler domain in the near field from the wave-equation domain in the far field.

Figure 3 shows contours of the instantaneous pressure field from the simulation. It is worth observing that smooth solutions are obtained near the coupling surface. In Fig. 4, the rms pressure from the scattered wave is compared with the analytical solution from inviscid theory and the rms pressure agrees with the theoretical results, with no indication of inaccuracies near the coupling interface. This test case demonstrates that our multimodel approach can accurately predict the intensity and directionality of acoustic wave scattered from a solid body. This and other validation cases reported in [30] provide confidence in the multimodel formulation.

BVI Model Problem

This section presents results for the optimal control of noise produced by the interaction of a vortex with a Bell AH1 rotor blade in a uniform freestream. For this BVI problem, as shown in Fig. 5, the computational domain is decomposed into three parts. In the middle region, the Navier–Stokes equations are used to model the nonlinear interaction between the vortex and rotor blade. In the upper and lower regions, the linearized Euler equations are used to capture the scattered acoustics. This domain is discretized with 4608 quadrilateral elements. Taking advantage of the local hp-refinement capabilities of the DG method, we use different polynomial orders in the near-field viscous region, and in the far-field linear acoustic region, with $p = 5$ used along the vortex trajectory and $p = 3$ used elsewhere, as shown in Fig. 6. Such local hp refinement not only gives more accurate representation of the localized phenomena, such as the vortex and boundary layer, but also improves the overall computational efficiency compared with a uniform polynomial order (see the subsequent discussion for more details on computational savings).

In the following, the freestream velocity and the chord length of the Bell AH1 rotor blade are used for nondimensionalization, which leads to the blade Reynolds number $Re = 1000$. The initial condition is computed by superimposing a relatively strong Oseen vortex of circulation -0.5 and core radius $R_v = 0.15$ on the steady-state solution of the Navier–Stokes equations for a uniform flow of freestream Mach number $M_\infty = 0.3$ over the Bell AH1 rotor blade. The vortex is advected downstream by the freestream and interacts with the rotor blade in its path, leading to a BVI-type noise source. To allow the initial transient acoustic waves to leave the domain, we advance the solution for 5.52 time units and define this as our initial condition for optimization ($t_0 = 5.52$).

Recall that the control objective (4) is to minimize the acoustic pressure intensity in the rectangular area depicted in Fig. 5. Motivated by the success of Collis et al. [29] using transpiration boundary for the optimal control of aeroacoustic noise generated by a vortex interacting with a circular cylinder, we use the time- and space-dependent distribution of surface normal velocity (suction/blowing)

over the entire rotor surface as our control mechanism. Nakamura's work [46] indicates that the leading edge of the rotor blade plays a very important role in the interaction process. Likewise, through numerical simulation, Morvant [47] also shows that BVI is primarily a leading-edge phenomenon and the compressibility waves that propagate upstream above and below the rotor are generated from the large flow deflections at the leading edge. These cited studies justify the use of transpiration as our control mechanism. Although the previous studies indicate that transpiration near the leading edge is most important, we allow for transpiration over the entire blade surface and allow the optimization procedure to determine where the control is most effective.

Based on these observations, we define our optimization time window to capture only the leading-edge acoustics, to reduce computational cost. Thus, the optimization time window consists of 20,000 uniform time steps, with $\Delta t = 8 \times 10^{-5}$ from time $t_0 = 5.52$ to $t_f = 7.12$. Four measurement stations are placed above and below the rotor blade to record the time history of pressure fluctuations (see Fig. 5).

Stations P_1 and P_2 are located in the linearized Euler subdomain above the blade to capture the upward traveling acoustic waves, and stations P_3 and P_4 are located inside the observation region Ω_{obs}. Contours of scattered pressure at different time instants are shown in Fig. 7, both with and without control. With control, the intensity of acoustic pressure inside the observation region is reduced dramatically. Quantitatively, the value of the objective function J is reduced from 0.91 to 0.06, and the sound pressure level in the observation region is reduced by approximately 12 dB.

However, the sound pressure level above the rotor blade upstream is slightly strengthened, as seen in Fig. 7, and this is consistent with previous results for a circular cylinder [29]. The changes in sound pressure levels are more clearly observed in Fig. 8, which plots the history of pressure fluctuations at stations P_1, P_2, P_3, and P_4. Compared with the uncontrolled pressure fluctuations at those four stations, the amplitude at P_3 and P_4 inside the observation region Ω_{obs} is noticeably reduced. Near the end of the time interval at P_4 there is a slight increase in the amplitude of the pressure fluctuations that is associated with acoustic waves generated as the vortex passes over the trailing edge of the rotor blade. Comparing the pressure fluctuations for uncontrolled and controlled flow in Fig. 8 shows that there is a delayed effect of the control observed at all stations, due to the finite sound speed.

In analyzing the space–time control distributions, we find that the control distribution is, in fact, nonzero over much of the airfoil surface, including near the trailing edge at early times. However, the most active control region is near the leading edge and the maximum transpiration amplitude is only 1% of the freestream velocity, which is considerably smaller than reported by Collis et al. [29], in which control was limited to a small region near the leading edge for a cylinder–vortex interaction problem. Our current optimization methodology provides a framework to explore many other control options, including limiting the spatial extent of the control and exploring different control mechanisms (synthetic jets, wall-tangent control, etc.).

Adjoint Analysis

To better understand the effect of wall-transpiration control, the evolution of adjoint variable λ_4 (in the near field) and ξ_4 in the far field, which contributes to the gradient information for the control update, is shown in Fig. 9. This adjoint quantity is associated with an adjoint acoustic wave generated by pressure fluctuations in the observation region. As the adjoint wave moves outward from the observation region, it interacts with the rotor blade, leading a nonzero adjoint field on the blade surface that corresponds to the gradient of the objective function with respect to the control. Given this qualitative behavior of the adjoint solution, such interaction between the control and the flowfield alters the far-field acoustics delicately by changing the near-field acoustic source. Figure 9 also shows that the adjoint solution around the coupling surface is quite smooth, indicating that our coupling approach for the adjoint equation is working properly.

Discussion

To understand the underlying mechanism of noise reduction, we consider the effect of the control on several important BVI parameters. Interestingly, two important parameters for BVI noise, vortex strength and miss distance, are not significantly changed. Without control, the vortex strength changes from -5.01 to -4.13 after passing the blade. With control, the vortex strength changes from -5.01 to -4.11 and the path is nearly identical, as shown in Fig. 10. Thus, the control appears to have a negligible effect on both the vortex trajectory and vortex strength.

Considering the direct relation between the strength of BVI noise levels and temporal pressure gradients near the leading edge [48], we now explore the effect of control on the transient drag and lift histories. Figure 11 shows that the drag coefficient C_d is slightly decreased during the first half of the optimization interval, which appears to be associated with the change in viscous stress due to the control on the rotor blade surface. During the second half of the optimization time interval, there are only slight changes in the drag, because the control is relatively weaker. This result suggests that the

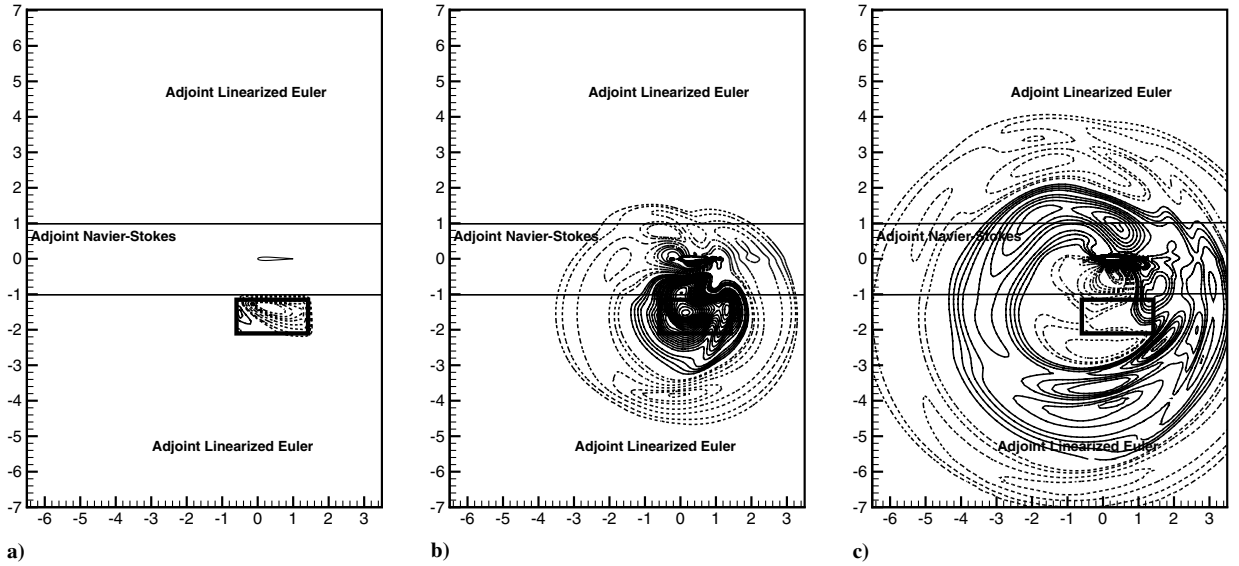

Fig. 9 Adjoint variable λ_4 in the near field and ξ_4 in the far field; time goes backward in the adjoint solutions a) $t = 7.12$, b) $t = 6.32$, and c) $t = 5.56$; contour increments are ± 0.17253; positive (solid lines) and negative (dashed lines).

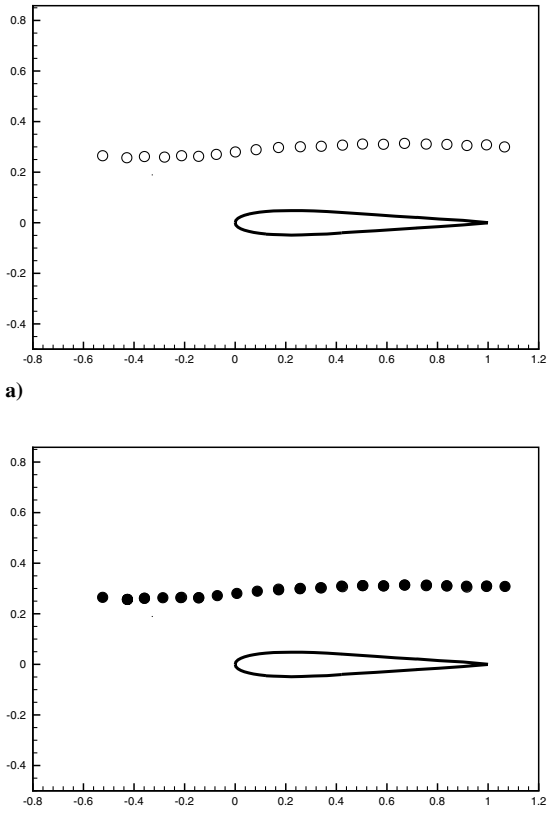

Fig. 10 Vortex trajectories: a) without control and b) with control.

primary BVI control mechanism targeted by the optimal control is largely inviscid. Although this fact is perhaps not surprising, given the largely inviscid nature of BVI sound generation, it is reassuring to know that given the possibility of a vortical control mechanism (such as generation of a counter-rotating vortex), the optimal control mechanism is, in fact, inviscid in nature.

The largely inviscid nature of both BVI noise and the resulting optimal control are clearly observed in the section lift coefficient C_l, which is primarily due to pressure differences on the blade surface. As observed by Peake and Crighton [49], the reduction of unsteady lift on the blade during a BVI event should, at least at low Mach numbers, lead to reduced sound generation. This observation has led to the use of oscillating trailing-edge flaps [50–52], as well as suction/blowing on the blade surface [53,54], to reduce the unsteady lift on rotor blades. Figure 12 shows that unsteady lift is noticeably

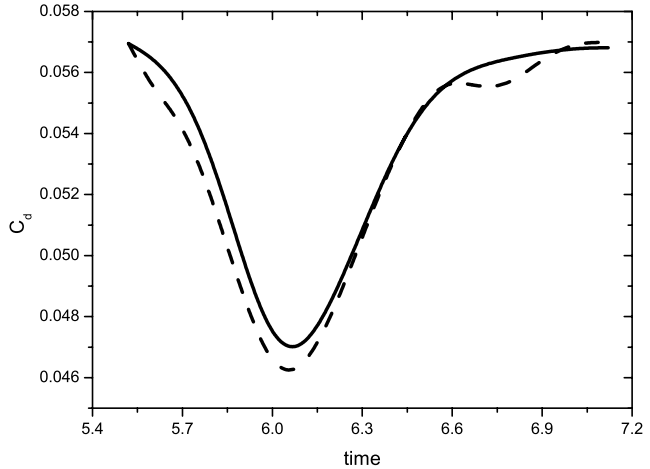

Fig. 11 Time history of drag coefficient C_d; no control (solid line) and optimal control (dashed line).

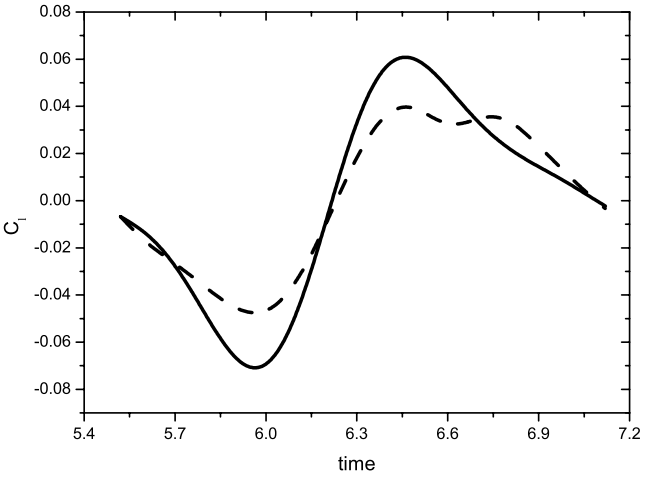

Fig. 12 Time history of lift coefficient C_l; no control (solid line) and optimal control (dashed line).

reduced due to the optimal control. Figure 12 also shows that the temporal gradient of C_l is reduced from approximately 0.3151 to 0.2148, which is directly related to the strength of BVI sound [48] due to the inviscid mechanism and is consistent with the results shown in Fig. 8.

We conclude with a few remarks regarding the efficiency of the multimodel/multidomain approach introduced here. For the BVI model problem considered here, approximately 40% of the elements are solved using the Navier–Stokes equations, whereas the remaining 60% are solved using the linearized Euler equations. The computational cost of the linearized Euler equations is approximately 50% of the cost associated with the Navier–Stokes equations, although the actual cost depends on the polynomial order of each element. Based on this, for the BVI proof-of-concept problem presented here (with variable element order as used in this problem), we expect an ideal savings of 27.5%. In practice, we obtain a 24% savings in computational time, where the additional 3.5% is due to the modest overhead incurred in the multimodel coupling. In the future, we plan to apply this approach to problems with much larger far-field regions, including three-dimensional problems. In these problems, the ratio of element in the near field to those in the far field will be smaller, asymptotically leading to a 50% savings. It is also important to remember that the storage required for transient optimization scales with the size of the nonlinear near field, and so the multimodel approach also dramatically reduces storage requirements for the adjoint solve. Reference [30] presents a far-field approach using a wave equation that is roughly 25% of the expense of a Navier–Stokes solve, leading to additional computational savings that we plan to exploit in future work. In addition, because of the high resolution required to resolve the viscous boundary layer near the blade in the near field and the associated small time steps with current explicit advancement scheme, the blade Reynolds number is limited to approximately 10^4 for a two-dimensional BVI control problem with a reasonable optimization time window. More realistic BVI control problems at higher Reynolds numbers will require some form of near-field turbulence model (or an inviscid approximation when appropriate) along with implicit time advancement.

Conclusions

To the best of our knowledge, we believe that this work is the first model-based effort using optimal control theory to construct controls that reduce blade–vortex-interaction (BVI) noise on a (relatively) realistic BVI configuration. Our solutions are obtained using an efficient and novel multidomain and multimodel method based on a high-order-accurate discontinuous Galerkin spatial discretization. This approach works well for both state and adjoint computations and leads to BVI control results that are quite promising. In particular, it is shown that optimal distributions of wall-normal suction and blowing can be obtained that significantly reduce

downward-radiated BVI noise. For the conditions studied here, a 12-dB reduction in sound pressure level is obtained when the objective function targets downward-radiated BVI sound. Although the optimal control has negligible effect on both the vortex strength and trajectory, it does alter the interaction of the vortical and potential fields, which is the source of BVI noise. Although this results in a slight decrease in drag, there is a significant reduction in the temporal gradient of lift, leading to a reduction in BVI sound levels.

Acknowledgments

Sandia is a multiprogram laboratory operated by Sandia Corporation, a Lockheed Martin Company, for the U.S. Department of Energy's National Nuclear Security Administration under contract DE-AC04-94AL85000. This work is partially supported by Texas Advanced Technology Program grant 003604-0011-2001, National Science Foundation (NSF) grant 0116289- 2001, and the U.S. Department of Energy. Some computations were performed on the Rice Terascale Cluster funded by NSF under grant EIA-0216467, Intel, and Hewlett-Packard. The authors have benefited from helpful discussions with Kaveh Ghayour and Matthias Heinkenschloss of Rice University and with Bart van Bloemen Waanders and Roscoe Bartlet of Sandia National Laboratories. The careful reading and the constructive comments of the two anonymous referees are also greatly appreciated.

References

[1] Collis, S. S., Ghayour, K., and Heinkenschloss, M., "Optimal Control of Aeroacoustics: Transpiration Boundary Control," *AIAA Journal*, Vol. 41, No. 7, July 2003.

[2] Chen, G., and Collis, S. S., "Toward Optimal Control of Aeroacoustic Flows Using Discontinuous Galerkin Discretizations," AIAA Paper 2004-0364, Jan. 2004.

[3] Leverton, J. W., and Taylor, F. W., "Helicopter Blade Slap," *Journal of Sound and Vibration*, Vol. 4, No. 3, 1966, p. 345. doi:10.1016/0022-460X(66)90132-5

[4] Schmitz, F. H., and Boxwell, D. A., "In Flight Far-Field Measurement of Helicopter Impulsive Noise," *Journal of the American Helicopter Society*, Vol. 21, No. 4, 1976.

[5] Boxwell, D. A., and Schmitz, F. H., "Full-Scale Measurements of Blade–Vortex Interaction Noise," *Journal of the American Helicopter Society*, Vol. 27, No. 4, 1982.

[6] Martin, R. M., and Splettstoesser, W. R., "Blade-Vortex Interaction Acoustic Results from a 40% Model Rotor in the DNW," *Journal of the American Helicopter Society*, Vol. 33, No. 1, 1988.

[7] Widnall, S. E., "Helicopter Noise Due to Blade-Vortex Interactions," *Journal of the Acoustical Society of America*, Vol. 50, No. 1, 1971.

[8] Caradonna, F. X., and Isom, M. P., "Subsonic and Transonic Potential Flow over Helicopter Rotor Blades," *AIAA Journal*, Vol. 10, No. 12, 1972, pp. 1606–1612.

[9] Summa, J. M., "Potential Flow About 3-Dimensional Lifting Configurations with Applications to Wings and Rotors," AIAA Paper 75-126, 1975.

[10] Arieli, R., and Tauber, M. E., "Computation of Subsonic and Transonic Flow over Helicopter Rotor Blades," AIAA Paper 79-1667, 1979.

[11] George, A., and Lyrintzis, A., "Acoustics of Transonic Blade-Vortex Interactions," *AIAA Journal*, Vol. 26, 1988, pp. 769–776.

[12] Lyrintzis, A., and Xue, Y., "Study of the Noise Mechanisms of Transonic Blade-Vortex Interactions," *AIAA Journal*, Vol. 29, No. 10, 1991, pp. 1562–1572.

[13] Xue, Y., and Lyrintzis, A. S., "Rotating Kirchhoff Method for Three-Dimensional Transonic Blade-Vortex Interaction Hover Noise," *AIAA Journal*, Vol. 32, No. 7, 1994, pp. 1350–1359.

[14] Yu, W. S., and Lakshminarayana, B., "Numerical Simulation of the Effects of Rotor-Stator Spacing and Wake/Blade Count Ratio on Turbomachinery Unsteady Flows," *Journal of Fluids Engineering*, Vol. 117, No. 4, 1995, pp. 639–646. doi:10.1115/1.2817316

[15] Krishnamoorthy, S., and Marshall, J. S., "Three-Dimensional Blade-Vortex Interaction in the Strong Vortex Regime," *Physics of Fluids*, Vol. 10, No. 11, 1998, pp. 2828–2845. doi:10.1063/1.869805

[16] McCluer, M. S., "Helicopter Blade-Vortex Interaction Noise with Comparisons to CFD Calculations," NASA Ames Research Center TM-110423, Moffett Field, CA, 1996.

[17] Brentner, K. S., and Farassat, F., "An Analytical Comparison of the Acoustic Analogy and Kirchhoff Formulation for Moving Surfaces," *American Helicopter Society 53rd Annual Forum*, AHS International, Alexandria, VA, 1997.

[18] Lyrintzis, A., "Review: The Use of Kirchhoff's Method in Computational Aeroacoustics," *Journal of Fluids Engineering*, Vol. 116, 1994, pp. 665–676.

[19] Farassat, F., "The Kirchhoff Formulas For Moving Surfaces in Aeroacoustics: The Subsonic and Supersonic Cases," NASA, TM 110285, 1996.

[20] Lighthill, M. J., "On Sound Generated Aerodynamically, 1: General Theory," *Proceedings of the Royal Society of London A*, Vol. 211, 1952, pp. 564–587. doi:10.1098/rspa.1952.0060

[21] Williams, J. F., and Hawkings, D., "Sound Generation by Turbulence and Surfaces in Arbitrary Motion," *Philosophical Transactions of the Royal Society of London, Series A: Mathematical and Physical Sciences*, Vol. 264, No. 1151, 1969, pp. 321–342. doi:10.1098/rsta.1969.0031

[22] Viswanathan, K., and Sankar, L. N., "Toward the Direct Calculation of Noise: Fluid/Acoustic Coupled Simulation," *AIAA Journal*, Vol. 33, No. 12, 1995, pp. 2271–2279.

[23] Djambazov, G., Lai, C., and Pericleous, K., "Development of a Domain Decomposition Method for Computational Aeroacoustics," *DD9 Proceedings*, Wiley, New York, 1997.

[24] Djambazov, G., Lai, C., and Pericleous, K., "Efficient Computation of Aerodynamic Noise," *Contemporary Mathematics*, Vol. 218, 1998, pp. 506–512.

[25] Djambazov, G., Lai, C., and Pericleous, K., "Staggered-Mesh Computation for Aerodynamic Sound," *AIAA Journal*, Vol. 38, No. 1, 2000, pp. 16–21.

[26] Collis, S. S., Ghayour, K., Heinkenschloss, M., Ulbrich, M., and Ulbrich, S., "Towards Adjoint-Based Methods for Aeroacoustic Control," AIAA Paper 2001-0821, 2001.

[27] Collis, S. S., Ghayour, K., Heinkenschloss, M., Ulbrich, M., and Ulbrich, S., "Numerical Solution of Optimal Control Problems Governed by the Compressible Navier–Stokes Equations," *Optimal Control of Complex Structures*, International Series of Numerical Mathematics, Vol. 139, Birkhäuser Verlag, Basel, Switzerland, 2001, pp. 43–55.

[28] Collis, S. S., Ghayour, K., Heinkenschloss, M., Ulbrich, M., and Ulbrich, S., "Optimal Control of Unsteady Compressible Viscous Flows," *International Journal for Numerical Methods in Fluids*, Vol. 40, No. 11, 2002, pp. 1401–1429. doi:10.1002/fld.420

[29] Collis, S. S., Ghayour, K., and Heinkenschloss, M., "Optimal Control of Aeroacoustic Noise Generated by Cylinder Vortex Interaction," *International Journal of Aeroacoustics*, Vol. 1, No. 2, 2002, pp. 97–114. doi:10.1260/147547202760236923

[30] Chen, G., "Multimodel Simulation for Optimal Control of Aeroacoustics," Ph.D. Thesis, Mechanical Engineering and Materials Science, Rice Univ., Houston, TX, 2004.

[31] Joslin, R. D., Gunzburger, M. D., Nicolaides, R. A., Erlebacher, G., and Hussaini, M. Y., "Self-Contained Automated Methodology for Optimal Flow Control," *AIAA Journal*, Vol. 35, No. 5, 1997, pp. 816–824.

[32] Hager, W. W., "Runge-Kutta Methods in Optimal Control and Transformed Adjoint System," *Numerische Mathematik*, Vol. 87, No. 2, 2000, pp. 247–282. doi:10.1007/s002110000178

[33] Hu, F. Q., Hussaini, M. Y., and Rasetarinera, P., "An Analysis of the Discontinuous Galerkin Method for Wave Propagation Problems," *Journal of Computational Physics*, Vol. 151, 1999, pp. 921–046.

[34] Rasetarinera, P., Hussaini, M. Y., and Hu, F. Q., "Some Remarks on the Accuracy of the Discontinuous Galerkin Method," *Discontinuous Galerkin Methods: Theory, Computation, and Applications*, edited by B. Cockburn, G. E. Karniadakis, and C.-W. Shu, Lecture Notes in Computational Science and Engineering, Vol. 11, Springer, New York, 2000, pp. 407–412.

[35] Atkins, H. L., and Lockard, D. P., "A High-Order Method Using Unstructured Grids for the Aeroacoustic Analysis of Realistic Aircraft Configurations," AIAA Paper 99-1945, 1999.

[36] Bismuti, P. J., and Kopriva, D. A., "Solution of Acoustic Scattering Problems by a Staggered Grid Spectral Domain Decomposition Method," *Second Computational Aeroacoustics (CAA) Workshop on Benchmark Problems*, NASA-CP-3352, NASA Langley Research Center, Hampton, VA, June 1997, pp. 69–78.

[37] Cockburn, B., Karniadakis, G., and Shu, C.-W. (eds.), *Discontinuous Galerkin Methods: Theory, Computation, and Applications*, Springer, New York, 2000.

[38] Cockburn, B. (ed.), "High-Order Methods for Computational Applications," *Discontinuous Galerkin Methods for Convection Dominated Problems*, Lecture Notes in Computational Science and Engineering, Springer, Berlin, 1999, pp. 69–224.

[39] Bassi, F., and Rebay, S., "A High-Order Accurate Discontinuous Finite Element Method for the Numerical Solution of the Compressible Navier–Stokes Equations," *Journal of Computational Physics*, Vol. 131, No. 2, 1997, pp. 267–279. doi:10.1006/jcph.1996.5572

[40] Abergel, F., and Temam, R., "On Some Control Problems in Fluid Mechanics," *Theoretical and Computational Fluid Dynamics*, Vol. 1, No. 6, 1990, pp. 303–325. doi:10.1007/BF00271794

[41] Berggren, M., "Numerical Solution of a Flow-Control Problem: Vorticity Reduction by Dynamic Boundary Action," *SIAM Journal on Scientific Computing*, Vol. 19, No. 3, 1998, pp. 829–860. doi:10.1137/S1064827595294678

[42] Chang, Y., "Reduced Order Methods for Optimal Control of Turbulence," Ph.D. Thesis, Mechanical Engineering and Materials Science,Rice Univ., Houston, TX, 2000.

[43] Morse, P. M., and Ingard, K. U., *Theoretical Acoustics*, Princeton Univ. Press, Princeton, NJ, 1968, pp. 400–405.

[44] Collis, S. S., and Lele, S. K., "A Computational Approach to Swept Leading-Edge Receptivity," AIAA Paper 96-0180, 1996.

[45] Tezduyar, T. E., "Stabilized Finite Element Formulations for Incompressible Flow Computations," *Advances in Applied Mechanics*, Vol. 28, 1992, pp. 1–44.

[46] Nakamura, Y., "Prediction of Blade Vortex Interaction from Measured Blade Pressure," *Vertica*, Vol. 6, No. 4, 1981, pp. 295–309.

[47] Morvant, R., "The Investigation of Blade-Vortex Interaction Noise Using Computational Fluid Dynamics," Ph.D. Thesis, Univ. of Glasgow, Glasgow, Scotland, U.K., 2004.

[48] Schmitz, F. H., Boxwell, D. A., Lewy, S., and Dahan, C., "Model- to Full-Scale Comparisons of Helicopter Blade-Vortex Interaction Noise," *Journal of the American Helicopter Society*, Vol. 29, No. 2, Apr. 1984, pp. 16–25.

[49] Peake, N., and Crighton, D. G., "Active Control of Sound," *Annual Review of Fluid Mechanics*, Vol. 32, 2000, pp. 137–164. doi:10.1146/annurev.fluid.32.1.137

[50] Kerschen, E. J., "Active Aerodynamic Control of Wake-Airfoil Interaction Noise Theory," Deutschen Gesellschaft für Luft- und Raumfahrt Paper 92-02-039, 1992.

[51] Simonich, J. C., Lavrich, P., Sofrin, T. G., and Topol, D. A., "Active Aerodynamic Control of Wake-Airfoil Interaction Noise-Experiment," Deutschen Gesellschaft für Luft- und Raumfahrt Paper 92-02-038, 1992.

[52] Parameswaran, V., and Baeder, J., "Reduction of Blade Vortex Interaction Noise Using Prescribed Pitching," AIAA Paper 1995-1891, 1995.

[53] Lee, S., "Reduction of Blade-Vortex Interaction Noise Through Porous Leading Edge," *AIAA Journal*, Vol. 32, No. 3, 1994, pp. 480–488.

[54] Hassan, A. A., Straub, F. K., and Charles, B. D., "Effects of Surface Blowing/Suction on the Aerodynamics of Helicopter Rotor Blade-Vortex Interactions (BVI): A Numerical Simulation," *Journal of the American Helicopter Society*, Vol. 42, No. 2, 1997, pp. 182–194.

E. Livne
Associate Editor